A computationally efficient finite element model for the analysis of the non-linear bending behaviour of a dynamic submarine power cable

Fabien Ménard, Patrice Cartraud

A computationally efficient finite element model for the analysis of the non-linear bending behaviour of a dynamic submarine power cable

Fabien Ménard, Patrice Cartraud

Nantes Université, Ecole Centrale Nantes, CNRS, GeM, UMR 6183, F-44321 Nantes, France

Abstract

This paper proposes a numerical approach based on a detailed 3D FE model to calculate the global mechanical behaviour and local stress state of dynamic submarine power cables. The method is applied to a three-core dynamic submarine power cable under a cyclic bending load. The numerical approach is based on the homogenization theory of periodic structures. The 3D computational domain is thus reduced to the helical period of the internal cable components, which allows the geometrical complexity and contact interactions between the components to be fully considered. In addition, the mesh size is reduced by using beam element modelling of the armour components. The study investigates the sensitivity of the cable bending behaviour to frictional interactions and manufacturing residual stresses. To validate the numerical model, the results are compared with experimental data and analytical results. The first comparison focuses on the overall behaviour of the cable under a cyclic bending load, while a local analysis compares quantities such as displacement and stresses with the results of analytical models available in the literature. The close agreement between the numerical, experimental and analytical results demonstrates the accuracy of the model in predicting the non-linear bending behaviour and local stresses that are essential for the cable design process.

Keywords: Dynamic power cable, Bending, Homogenization, Finite element method, Contact

1 Introduction

Dynamic submarine cables or umbilicals are widely used in the offshore industry, particularly in renewable energy systems. These cables are deployed in floating systems such as wave energy converters or, as presented in this article, in the case of floating wind turbines. The dynamic power cable is a key component of a floating wind turbine as its main role is to transport the electrical energy generated by the turbine to the electrical grid. The cable also plays a crucial role in managing the communication and data exchange between the different subsystems of the wind turbine and the control centre. Dynamic power cables are complex and heterogeneous structures composed of several metallic components: copper or aluminium in the centre of the power cores (conductive part), and steel on its periphery

(armour layers). These metallic components consist of a helically wound arrangement of wires creating concentric layers. The components are protected by plastic sheaths and held together by filling in the gaps around them. The dynamic cable is immersed and deployed over several tens of metres between the floating platform and the seabed, see Figure 1a. During service, the cable is mechanically constrained by the movement of the platform, swell and current movement, which ultimately expose the cable components to mechanical fatigue, particularly in the case of cyclic bending loading [1].

Designing cables involves calculating their response in service. From a mechanical point of view, the cable time response is determined at different sea states. In such an analysis, the cable is described by a numerical beam model subjected to hydrodynamic loads and platform motions, see [2–6]. It is therefore important to provide the stiffness characteristics of the beam to this model. It is also necessary to estimate the local stresses in the cable components from the results of the beam model to perform a fatigue analysis. The overall behaviour of the beam and the local stress state can be obtained by different approaches.

The axisymmetric behaviour (traction and torsion) of the cable is generally well predicted thanks to the several analytical or numerical models present in the literature. An expression of the stiffness in tension and in torsion is given in [7] based on the curved beams theory. A more precise formulation of the axial response is given in [8] which takes into account the material non-linearity, the contact and the local curvature variation of the helical strands. A finite element (FE) formulation of the axial problem is developed in [9], based on curved beam kinematics and the thin shell theory. A 3D FE modelling is proposed in e.g. [10–13] which shows a good agreement between analytical and numerical predictions.

However, compared to the axial case, few bending analyses are present in the literature. This is mainly due to the non-linear behaviour resulting from friction and sliding between components, which depend on the initial strain and stress state of cables, as shown in the experimental studies in [14, 15]. In [16] an analytical approach is proposed to estimate the armour layers bending stiffness. Expressions are given in slip behaviour where all components are free to slip in the cable cross-section and in stick behaviour where no slip is possible. The formulation is based on a discrete curved beam description of the helical components, see [17–19]. An analytical formulation using the principle of minimum strain energy is proposed in [20] to evaluate the bending behaviour of flexibles and umbilicals. In [21], an analytical formulation of the bending response is proposed to study the fatigue of the helical components. The radial contact pressure between layers is estimated from a numerical analysis of the axial loading case. The sliding of the components is described by a loxodromic curve. Other bending models use geodesic kinematics, see [22] in the case of flexible. A discussion of this hypothesis can be found in [23, 24].

As shown in [25], the limitations of the analytical models to account for contact, friction and sliding have lead many authors to use numerical models to characterise the bending behaviour and the stress state in power cables. In [26], UFLEX software is developed with a specific FE formulation based on curved beam kinematics, which shows a reasonable correlation between model and experimental tests for hysteresis bending cycle load. However, the model seems to overestimate stiffness, particularly in the initial phase of the stick state. In [27], the previous numerical tool is used to study the fatigue strength of power core

conductor. It is shown that the 3D approach allows for taking into account the local change of curvature due to the point contact distribution between the different strands layers. In [28], the non-linear bending behaviour of a copper conductor is analysed with a FE model with beam and shell elements solved with BFLEX, and compared to tests results. Other authors propose a 3D analysis by the FE method using commercial softwares such as ANSYS, ABAQUS. A 3D description with solid elements allows a detailed analysis of the behaviour and the stress state especially for simple metallic cable, see [29, 30]. However, it requires a large computation time for complex geometries encountered in dynamic cables. In [25], [31] and [32] beam or shell elements are used to save computation time while ensuring good accuracy in the stress state prediction within wires and components. However, the model axial length is taken sufficiently large to limit the edge effects generated with the use of rigid-body assumptions for the end cross-sections. In [3] the axial model is reduced to a representative part of the cable corresponding to the armours helix pitch. Each component is modelled with solid elements. The lay angle of the power cores is neglected and conductors are approached by continuous straight copper cylinders. The bending loads are applied through kinematic periodic boundary conditions connecting each component to a virtual beam which represents the cable main axis, see [33]. In [34] a representative part of the cable, corresponding to 1/3 of the lay length of the power cores is modelled with solid elements. The loads are applied through periodic boundary conditions. The penalty method and Coulomb regularisation are used to solve contact between the various components. An initial stress state is introduced into the model by applying pressure to the cable outer sheath. A similar approach is applied to flexible pipe in [35].

The objective of this paper is to propose a computationally efficient numerical approach to calculate the bending behaviour and the local stress state of dynamic submarine cables. To achieve this goal, the approach is based on a homogenization method initially proposed in [36] and used in a computational framework in [37]. It has recently been applied to metallic strands in [38, 39]. Thus, as in [3, 34] the size of the numerical model is reduced to the helical pitch of the internal components using specific periodic boundary conditions. In addition, the numerical model integrates beam elements to reduce the model size. Several parameters of the numerical model, such as the friction coefficient and the initial stress state are studied to highlight their influence on the pure bending behaviour, as in [28]. The numerical model is then compared to experimental results, focusing on a cyclic bending loading to draw comparisons on the overall cable behavior. A local analysis is also provided comparing quantities such as displacement and stresses to analytical results. The example considered is an 8MW three-core cable which is representative of the submarine power cables used in floating wind turbine farms.

2 Description of the mechanical problem

2.1 Global scale configuration

The submarine dynamic cable considered here is a three-core power cable with an external diameter of 101 mm. A bend stiffener tied to the platform is used at the hang-off section of

the cable, and the other end is connected to a static cable laid on the seabed. A lazy wave shape is considered with buoyancy modules around the cable.

The critical zones of interest, where the curvature variation is most significant, are the sagging and hogging zones as shown in see Figure 1a. Therefore, this paper is focused on the bending behaviour of the cable, although the proposed approach may be used for studying its axial - tensile and torsion - behaviour.

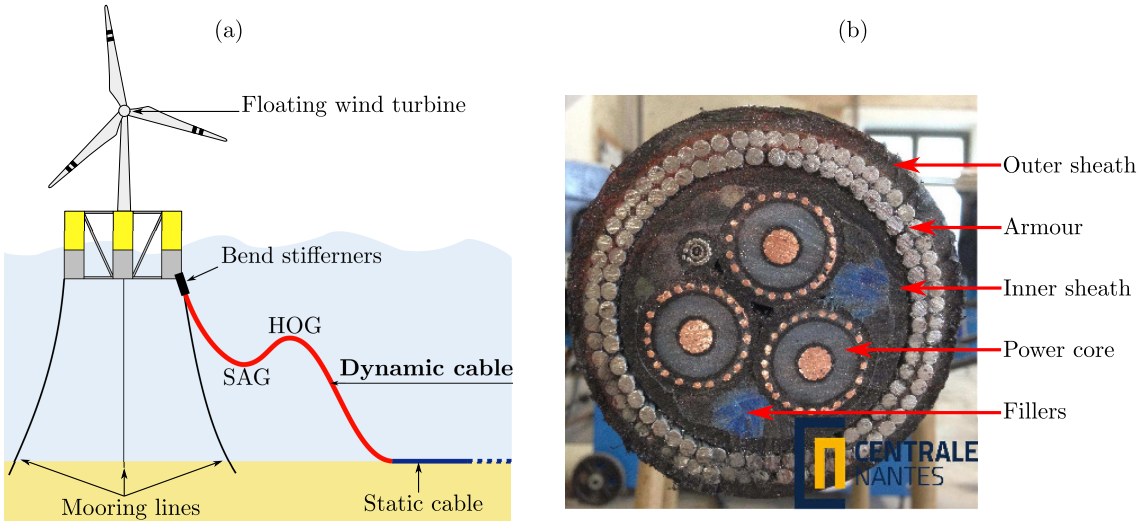

Figure 1: Representation of the lazy wave configuration for floating wind turbine application (a) the dynamic cable cross-section, photograph courtesy of Ecole Centrale Nantes (b)

2.2 Local description of the dynamic submarine power cable

In Figure 1b, a cross-sectional view of the three core power cable is shown, while Figure 2 illustrates its helical assembly. The cable comprises two armour layers of galvanised steel helical wires, with their lay angles arranged in opposite directions to minimise the tension-torsion coupling. The armour bedding is made of a single layer of perfluoro-elastomers (PFR), while the inner and outer sheaths are composed of high density polyethylene (HDPE). The stranded copper cores of the cable possess a helical mean line. The insulation system comprises an extruded layer of cross-linked polyethylene (XLPE) covered by helical copper wires and a HDPE insulation/power core shield. The fillers, which are made of polypropylene (PP) ropes, ensure circularity and concentricity of the cables. The fillers also contain a galvanised steel tube that is protected by steel wires and houses the optical fibres.

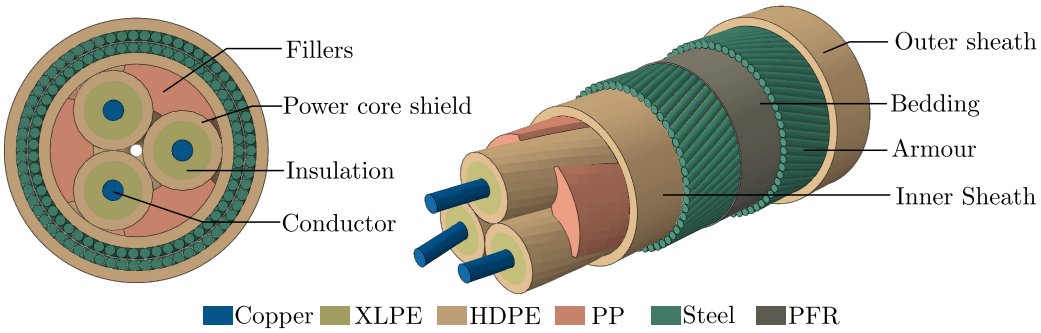

Figure 2: 3D Representation of cable geometry with the different components material

2.3 Mechanical behaviour of dynamic cables

The bending behaviour of the cable is strongly influenced by the contact interactions between its different components. During the manufacturing process, extrusion of external and internal sheaths generates an initial state with a non-zero normal contact force between the components, as reported in an experimental study in [15]. In conjunction with friction, this normal contact force causes the cable to exhibit a stick-slip bending behaviour of the cable. For small curvatures, no relative slip exists between the components and the bending stiffness is maximum $(EI)_{max}$, as shown by path OA in Figure 3. As the curvature increases, slip propagates throughout the entire cross-section until the minimum bending stiffness $(EI)_{min}$ is reached, shown by path BC in Figure 3. Typically, slip starts in the layer furthest from the cable main axis at the neutral axis and propagates towards the internal layers [18]. The size of the stick region depends on initial stresses resulting from manufacturing processes and the the tensile force. The latter increases the normal contact force between the components and, as a result, the size of the stick region.

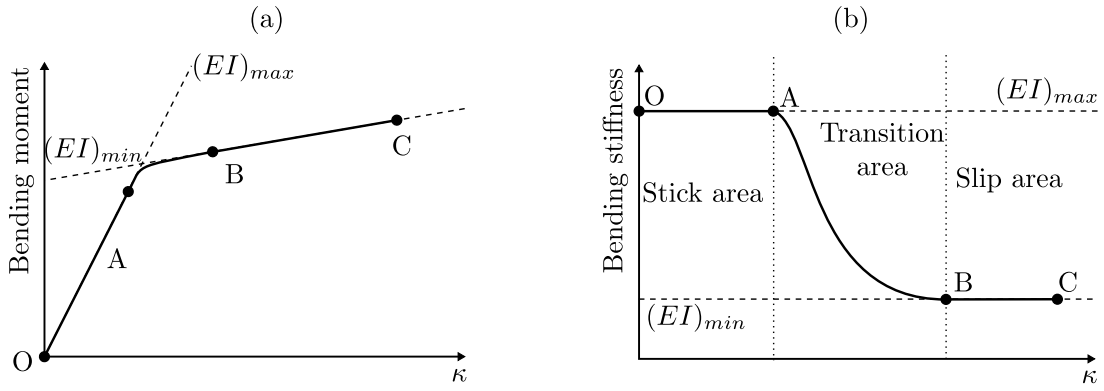

Figure 3: Representation of the bending moment as a function of curvature (a) and bending stiffness as a function of curvature (b)

3 Experimental study

In this study, the bending response of the dynamic cable is obtained by using a four point bending test. The tests were conducted at the Tony Davies High Voltage Laboratory

(TDHVL), located at the University of Southampton, England. The load is applied to the cable via two hydraulic actuators exerting a force F_a parallel to $\vec{y}$-axis, see Figure 4. Each actuator is placed at a distance L_1 from the ends of the bench, where L_1 represents a quarter of the total bench length: $L_g = 4L_1 = 2.5$ m. In contrast to a three-point bending, the choice of a four-point bending ensures a zero shear force between the 2 hydraulic actuators, which results in pure bending with a constant bending moment. The tests are performed in the horizontal plane $(\vec{x}, \vec{y})$ to avoid any influence from gravity on the results. A general view of the test bench is shown in Figure 5a.

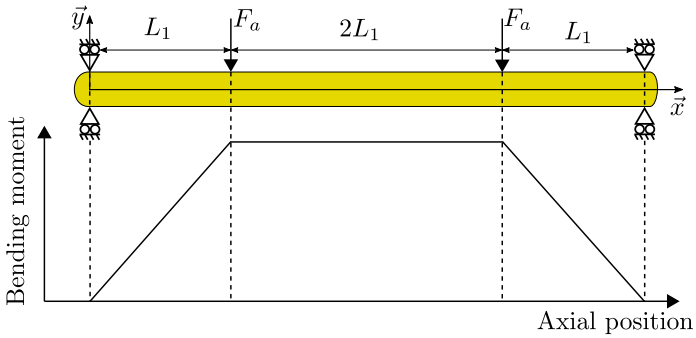

Figure 4: Representation of the four-point bending bench

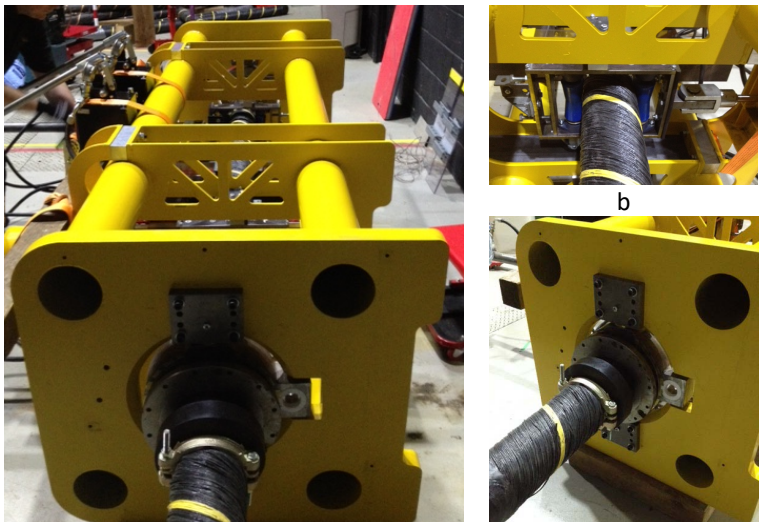

Figure 5: General view of test rig (a) ; roller interface between cable and actuators (b) ; linear bearing systems at pivoting ends (c), courtesy of Tony Davies High Voltage Laboratory, University of Southampton

3.1 Boundary conditions of the test bench

The cable is allowed to freely pivot and slide in translation into and out the ends of the test bench, as shown in Figure 5c. Thus, only the two hydraulic actuators can transmit a

shear force to the cable. The connection between the hydraulic actuators and the cable is made by roller interfaces, as shown in Figure 5b. The rollers are specific shaped to fit the cable outer sheath. This allows the cable to pass freely through the rollers without rotating around its own axis when an increasing bending moment is applied. To prevent bending due to the cable weight, it is supported by Perspex plates. Each plate is fixed to rails which allow the cable to move with it, minimising the frictional forces.

3.2 Force and displacement measurement

The force applied to the cable is measured from two load cells placed between the hydraulic actuators and the metal frame that holds the rollers and the cable. The cable displacement is measured at 5 points along the cable length, with 3 points between the two actuators. The measurement system is based on LVDT (Linear Variable Differential Transformer) sensors.

3.3 Bending behaviour

For this four point bending test, the bending moment M between the two actuators is given by:

$$M = F_a L_1 \tag{1}$$

The constant bending moment between the two actuators results in a constant curvature. This property can be used to calculate the curvature from the three LVDT measurements between the two actuators using two different methods. The first approach involves determining the coefficients of a second-order polynomial that describes the deflection between the two actuators using a least squares method. The curvature is then calculated as the second derivative of the polynomial. The second approach involves fitting an arc of a circle to the deformed shape of the beam between the two actuators using a least squares method, and calculating the curvature as the inverse of the circle radius. Both approaches were used, and the difference between the two curvature values obtained using them was found to be negligible.

3.4 The different measurement steps

Before the test, it is interesting to take into account the cable conditioning. The cable is stored around a drum with a constant curvature. Once unwound, the cable relaxes until it reaches equilibrium. Therefore, the first step in preparing the cable is to take a sample of the cable and lay it on a flat and horizontal surface to reduce the residual curvature accumulated during storage. The cable is then left on the test bench without external stress overnight to reach thermal equilibrium (20 ± 1.5 ° C). The cable is positioned with the residual curvature perpendicular to the bending plane (horizontal plane $(\vec{x}, \vec{y})$) to avoid its influence on bending behaviour. Under the effect of the weight and after relaxation, this residual curvature is thus close to 0 m $^{-1}$. A first bending cycle between -0.1 m $^{-1}$ and 0.1 m $^{-1}$ brings the cable to zero curvature and to an initial bending moment close to 0 N.m. Subsequently, several bending cycles are measured by alternating the direction of the hydraulic force and varying the amplitude of transverse displacement.

3.5 Bending cycles measured

The curvature ranges tested were chosen based on a compromise between the capacity of the bench, the minimum static breaking load and minimum dynamic breaking load. These ranges are realistic compared to those expected under operational conditions of the cable. The global reference model considers a floating wind turbine with an 8MW turbine per 60m of water in an exposed North Atlantic environment.

The curvatures considered correspond to the critical intermediate points: SAG and HOG zones, where the maximum curvature is 0.2 m $^{-1}$. The bending loading curve used for the mechanical characterisation test is shown in Figure 6. For each curvature level, 5 cycles of 5 minutes are performed. A bending cycle is considered sufficiently slow to neglect the viscoelastic effects and the initial moment is considered to be zero.

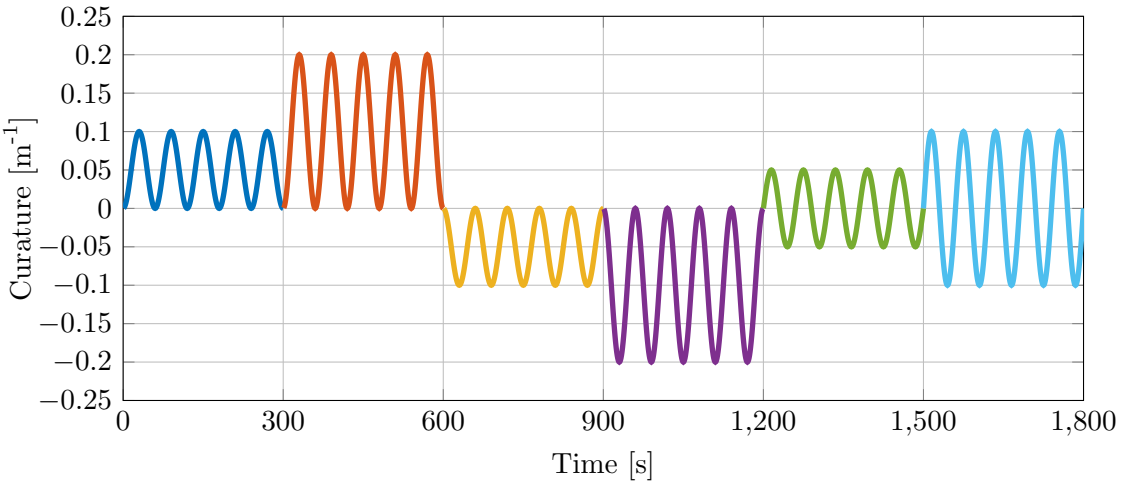

Figure 6: Loading path for the mechanical characterisation of the dynamic cable

3.6 Tests result example

A typical bending cycle obtained from the test for a curvature range of -0.10 to 0.10 m^{-1} is shown in Figure 7. The bending moment diagram exhibits a significant non-linearity that is due to the residual stress and strain present in the cable at the initial state. The stick state behaviour is observed after the change in direction of the force application. Following this change, the bending stiffness decreases until the slip state behaviour is reached.

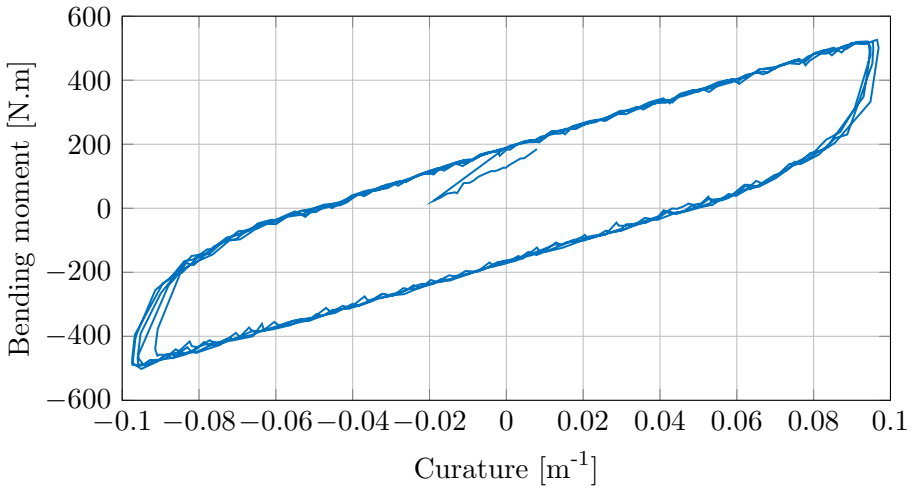

Figure 7: Bending moment-curvature diagram obtained from the test for a curvature range of -0.10 to 0.10 m^{-1}

4 Numerical model

In this paper, the bending behaviour measured by the test bench is used as a reference to assess a 3D FE model built with ABAQUS software. A detailed 3D description of the submarine dynamic cable with solid elements and the length of the cable under test would lead to prohibitive computation time. The homogenization method for periodic beams provides an efficient and rigorous means to reducing the size of the computational domain, given the structural axial periodicity, which stems from the helical geometry of cable components. Furthermore, the use of beam elements can also help reduce the size of the numerical model.

4.1 Model geometry

Several simplifications and assumptions are made to account for uncertainties in the initial cable geometry, particularly since the initial cable strain state at the end of the manufacturing process - which is unknown - can affect the geometry, particularly the contact surfaces between different components.

For instance, a single bedding is represented between the outer armours to simplify contact interaction between the two layers, with slightly increased thickness to prevent mesh distortion during loading. The fillers are modelled using a continuous material in polypropylene, and the tube containing the individual optical fibres is not included since it has a negligible influence on the cable response and is of minor interest for this study.

Each conductor wire has an irregular cross-section with a polygonal shape due to the manufacturing process, but the slip between conductor wires is disregarded. Therefore, the entire conductor is modeled as a uniform copper helix with a circular base. Screens, absorbent tapes and polyethylene sheaths of the insulation are not considered in the model.The geometrical data used in the numerical model correspond to the specimen that was tested and are presented in Table 1. The model representation is shown in Figure 2.

Name	Number	Material	Outer radius [mm]	Thickness [mm]	Helix Angle [deg]
Outer sheath	1	HDPE	50.5	4.5	–
Outer armour	63	Steel	2.0	–	19.6
Bedding	1	PFR	42.0	0.6	–
Inner Armour	55	Steel	2.00	–	-20.1
Inner sheath	1	HDPE	37.4	4.5	–
Power core shield	3	HDPE	15.3	4.0	9.0
Insulation	3	XLPE	11.3	7.3	9.0
Conductor	3	Copper	4.0	–	9.0
Fillers	3	PP	–	–	9.0

Table 1: Geometrical data of the cable cross-section

4.2 Periodic beams homogenization theory

Homogenization theory has been used in the past to study the structural analysis of periodic beams, see e.g. [36, 40, 37, 41]. This method has recently been applied to metallic strands with contact non-linearities [38, 39]. It provides an efficient and rigorous means of reducing the size of the computational domain by using the helical symmetry of the components. This allows for a fine discretisation and precise representation of the helical geometry of dynamic cables.

The cable is considered as slender structure with geometrical periodic heterogeneities along its main axis. The size of the computational domain is defined by the heterogeneities length, i.e. through a period which depends on the helical pitch and the number of components of each helical layer.

Assuming a single-layer cable, the period length l is defined by the periodic pitch p and the number n of helical components in the layer:

$$l = \frac{p}{n} = \frac{2\pi R_h}{ntan(\alpha)}, \tag{2}$$

where R_h is the layer mean radius and α the lay angle. An example of a period is given on Figure 8 for a 3-wire helical cable.

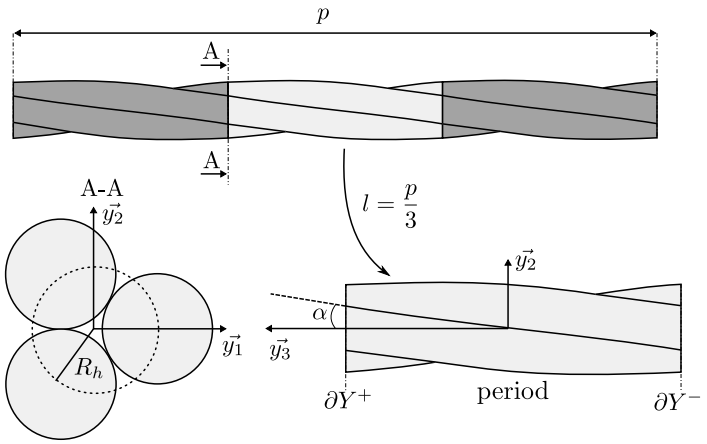

Figure 8: Representation of the period length in the case of a single layer 3-wire helical cable

As soon as cable is composed of several helical layers, the period length is defined by the common pitch between the different helical layers j and by the number n_j of components in a layer j:

$$l = k_j \frac{p_j}{n_j} = k_{j+1} \frac{p_{j+1}}{n_{j+1}} = ... = k_m \frac{p_m}{n_m}, \tag{3}$$

with $k_j \in \mathbb{N}$ and m the number of helical layers.

In the umbilical case and knowing the helical pitch of the two armour layers and the three cores, the model length is defined from the equation (3) such that:

$$l = 20\frac{p_1}{63} = 20\frac{p_2}{55} = \frac{p_3}{3}, \tag{4}$$

where the indices 1, 2 and 3 correspond to the outer armour layer, the inner armour layer and to the power core, respectively. The lay angle of the armour layers is adjusted slightly to obtain the same period length between layers. The deviation of the armour lay angle between the numerical model and the values measured on the cable is considered to be not significant (< 2 %) to affect the solution. The model data in Table 1 indicate that the period length of the proposed numerical model is 234.2 mm.

The homogenization approach, which is based on the asymptotic expansion method of the displacement field, decomposes the initial three-dimensional elasticity problem into microscopic three-dimensional elasticity problems written on the period and one-dimensional macroscopic problems corresponding to an Euler-Bernouilli beam problem that provides the overall beam response. The solution of the microscopic problems corresponds to the localisation step, which allows to relate the local strain and stress state to the macroscopic strains. The macroscopic strains are denoted by E^E, E^{F_1}, E^{F_2}, and E^T and correspond to the axial extension, curvatures and torsion rate, respectively, as shown in Figure 9. In the microscopic problem posed on the period, the displacement field is l-periodic in variable y_3, and the strain field and the stress field are obtained from the macroscopic strains as reported in [37].

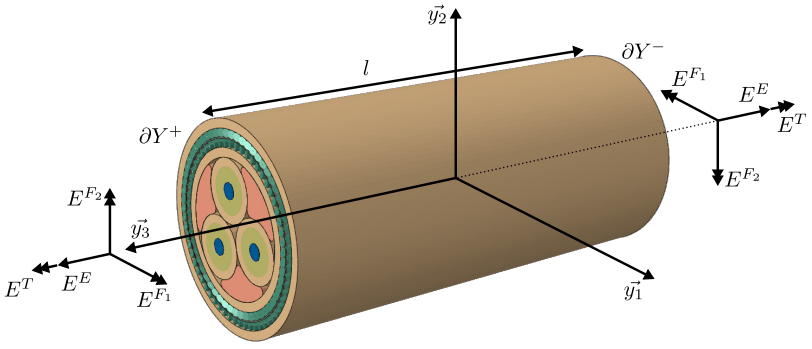

Figure 9: Representation of a dynamic cable period subjected to macroscopic strains

The numerical solution of the problem is computed using periodic boundary conditions and an l-periodic mesh in the FE model. The mathematical framework of this method is

well established in the case of components perfectly bonded together, as described in [36]. It is assumed herein that the same periodic boundary conditions can be applied in the case of a structure with several components and contact interactions, as presented in [38].

4.3 Components material

The elastic behaviour of each components is characterized by a Young modulus and a Poisson's ratio. Since no reference values were provided by the cable supplier, the values listed in Table 2 were obtained from various sources, including material databases and other studies such as [3] and [34].

Name	**Young's Modulus [MPa]**	**Poisson coefficient**
Steel	210000	0.3
Copper	110000	0.3
HDPE	1380	0.4
PP	1300	0.4
PFR	512	0.4
XLPE	350	0.4

Table 2: Elastic properties used in the FE model

4.4 Numerical model. Mesh and contact interactions.

The structure mesh is generated from a in-house program developed in MATLAB to ensure the mesh periodicity required for the homogenization method, as presented in [38]. The model mesh consists of several types of elements shown in Figure 10. The mesh generation is closely tied to the contact surface discretisation and the proposed approach for each component interaction is presented in this section.

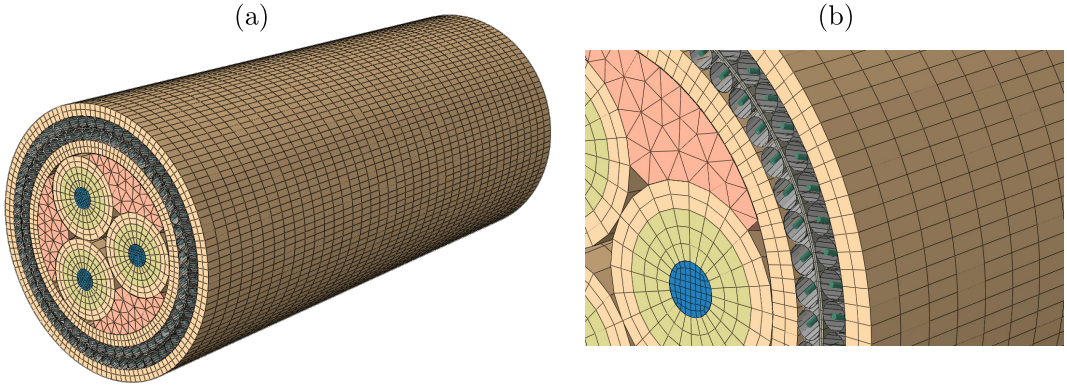

Figure 10: Display of the cable mesh: global view (a) and close-up view of the armours (b)

Given the large number of armour wires, each wire is modelled as a beam element with surface elements for contact modelling. As shown in [38], the coupling of beam and surface elements provides a very good compromise between accuracy and computational efficiency. The contact interactions between armour wires and outer sheath, inner sheath or bedding induce shear forces on beam elements. Therefore Timoshenko beam elements (B31

in ABAQUS) are used. The beam circumference is discretised with 4-node surface elements (SFM3D4 in ABAQUS), and rigid beams connect each surface node to the beam element nodes (Multipoint Constraints in ABAQUS). As a result the number of independent degrees of freedom is significantly lower than that of a solid element mesh. The sheaths and the power core are meshed with linear hexahedral solid elements (C3D8 in ABAQUS) and fillers are meshed with prism elements (C3D6 in ABAQUS). The use of homogenization theory to minimise the axial length of the computational domain results in a FE model of 142,920 elements.

Contact interactions arise between several components in the cable cross-section, including those between solid elements or solid elements and beams with surface elements. As shown in Figure 11, the contacts between solid elements are located in the inner part of the cable, i.e., filler with core, filler with inner sheath, core with core, core with conductor, and core with inner sheath. The radial contact between solid elements within the same armour layer is ignored, considering the mean radius and lay angle of armour wires. Consequently, the contacts between solid elements and beams with surface elements are between armour wires and outer sheath, bedding, and inner sheath.

The contact surface discretisation is dependent on the contact surface width between two components. Contacts between armour wires and plastic sheaths, as well as core-core and core-inner sheath contacts are approximated by a contact line. Therefore, a node-surface algorithm is chosen to reduce the size of the model and simplify the mesh, as shown in Figure 11. When contact surfaces cannot be approximated by a contact line, such as in the case of core-fillers, fillers-inner sheath, a surface-surface algorithm is adopted. It is assumed that the insulation is perfectly bonded to the power core shield.

However, to account for contact between the insulation and the conductor, referred to as IC contact, two assumptions are considered. The first, denoted Case 1 - pure stick IC contact interface, is a stick assumption which is modelled by a common node surface between the insulation and the conductors. The second, denoted Case 2 - frictional IC contact interface, is a frictional contact assumption that allows for relative displacement between the insulation and the conductors. This is modelled by a surface-surface contact algorithm. These two assumptions show no difference in the overall bending behaviour of the cable, but some differences can be noticed at the local scale, particularly with respect to axial stress, as discussed in the following.

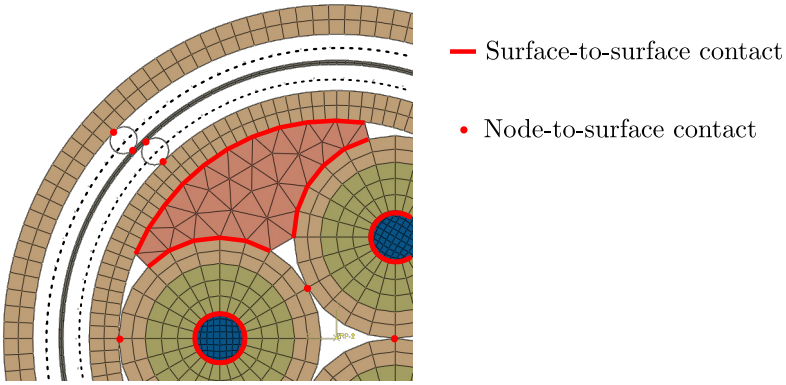

Figure 11: Display of a quarter of the cable mesh with contact surface discretisation

The element sizes were selected based on a convergence study of the cable homogenized bending stiffness. The resulting mesh, shown in Figure 10, achieves a good compromise between accuracy and computation time.

4.5 Contact modelling

Contact modelling is a critical aspect of model generation. It is necessary to model the contact force transmission between layers and the friction that causes the non-linear bending behaviour of the cable.

In preliminary studies conducted in [38], different methods of contact modelling were evaluated in the case of single and multilayer strands. The penalty method is used to solve normal and tangential contact. However, when dealing with a contact involving beams with surface elements, the contact surface has neither thickness nor stiffness. Consequently, it is necessary to combine the penalty method with the Lagrangian method to limit the penetrations and define the contact stiffness..

In the tangential direction, the penalty coefficient depends on the critical relative displacement which delineates the stick behaviour and the slip behaviour. The critical relative displacement is defined as a fraction β of the characteristic length l_e of the element in contact:

$$g_T^{crit} = \beta l_e. \tag{5}$$

As shown in [38], the bending behaviour is sensitive to the parameter β. A very small value β provides a good approximation of Coulomb's law but causes convergence issues. A larger value increases the slip, but makes the full slip regime occur too late. In the present work, the value $\beta = 0.001$ is chosen to ensure a good approximation of the Coulomb's law.

Regarding the slip between different cable components, the small sliding approach can be used as in [42] and [43], for metallic strands. The contact relationships are established only once in the first iteration of the computation, which saves computation time. A preliminary study showed that for a maximum curvature of 0.2 m $^{-1}$, there was a difference of less than 5% in terms of bending stiffness between small sliding and finite-sliding assumptions. Therefore, small sliding is used in this study.

4.6 Boundary conditions

The periodic homogenization problem is solved by the FE method with periodic boundary conditions. These periodic boundary conditions are expressed in terms of the macroscopic strains, which are shown in Figure 9. They lead to linear relations between each degree of freedom of two opposite nodes belonging to the boundary ∂Y^+ and ∂Y^-. The translation degrees of freedom of the boundaries, denoted U_i^+ and U_i^-, are related by the following equations [37]:

$$U_1^+ - U_1^- = l(\overline{y}_3 E^{F_1} - y_2 E^T), \tag{6}$$
$$U_2^+ - U_2^- = l(\overline{y}_3 E^{F_2} + y_1 E^T), \tag{7}$$
$$U_3^+ - U_3^- = l(E^E - y_\alpha E^{F_\alpha}), \quad \alpha = [1,2], \tag{8}$$

with $\overline{y}_3 = \dfrac{1}{2}(y_3^+ + y_3^-)$ and $y_\alpha = y_\alpha^+ = y_\alpha^-$.

For beams, three equations are added for the rotational degrees of freedom of the boundaries, denoted θ_i^+ and θ_i^- [44]:

$$\theta_1^+ - \theta_1^- = l E^{F_1}, \tag{9}$$
$$\theta_2^+ - \theta_2^- = l E^{F_2}, \tag{10}$$
$$\theta_3^+ - \theta_3^- = l E^T. \tag{11}$$

The FE problem can be written as:

$$[K] \left\{ \begin{array}{c} \{U\} \\ \left\{ \begin{array}{c} E^E \\ E^{F_1} \\ E^{F_2} \\ E^T \end{array} \right\} \end{array} \right\} = \left\{ \begin{array}{c} \{0\} \\ l \left\{ \begin{array}{c} N \\ M_1 \\ M_2 \\ M_3 \end{array} \right\} \end{array} \right\}, \tag{12}$$

where $[K]$ is the stiffness matrix. The loading case is defined by the corresponding values of macroscopic strains. Using equation (12), the axial force and the macroscopic moments are then obtained from the right-hand term. As shown in [38], it is assumed that these boundary conditions are valid even if the components are in contact. In that case, one set of boundary conditions is defined for each component.

4.7 Loading and simulation parameters

The loading process is divided into two steps: the initial state of the cable and cyclic bending loading. Each load step is summarised in Figure 12.

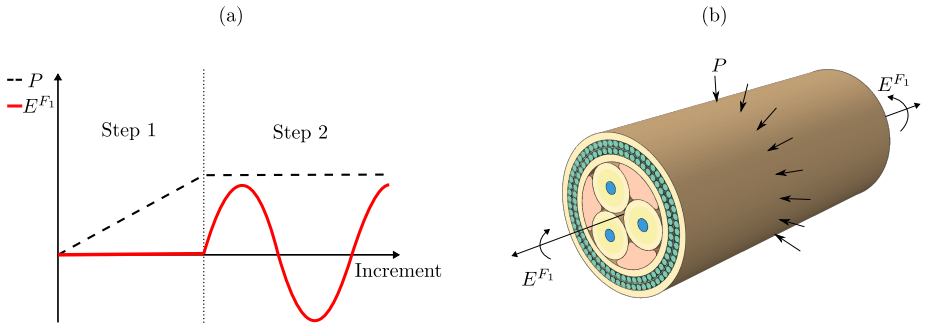

Figure 12: Representation of the different loading steps applied to the dynamic cable

The initial state arises from the manufacturing process which leads to a non-zero normal contact force between the different components of the cable, and the cable storage on a drum resulting in a non-zero residual curvature. In this study, only the initial state after the manufacturing process is considered, and is simulated with a uniform radial pressure P applied along the length of the external membrane, as suggested in [34]. The final pressure value is calibrated by comparing the numerical and experimental results, as explained in the following.

The second loading step consists of applying a sinusoidal curvature E^{F_1} around the $\vec{y_1}$-axis to represent the bending cycle, as shown in Figure 12, using the periodic boundary conditions, see equations (6) to (11) ($E^E = 0$; $E^{F_1} \neq 0$;$E^{F_2} = 0$;$E^T = 0$).

An implicit scheme is used to solve the FE static problem, with the number and size of the increments chosen based on the model size, loading and solution convergence speed. The friction in the numerical models results in a non-symmetry of the stiffness matrix, and therefore, a non-symmetrical storage of the stiffness matrix is used to obtain a converged solution.

The homogenization problem is solved assuming small displacements and small strains, which means that the displacements are small compared to the cable diameter.

The periodic homogenization problem solution is defined up to a rigid body displacement, which includes three translations and a rotation around the cable's main axis for each component. These displacements are dissipated with a viscous damping coefficient added to the implicit scheme, see [38]. To ensure a negligible effect on the final solution, this coefficient is updated throughout the simulation, keeping the ratio of damping energy to total energy less than 5%.

As discussed in section 4.4, the mesh consists of 142920 elements, including beam, surface and solid elements. The number of nodes is 165,148 and 168,100 in Case 1 - pure stick IC contact interface, and Case 2 - frictional IC contact interface, respectively. Since the surface element nodes of the beams and the nodes of the two end cross-sections are subjected to multipoint constraints, the total number of free dofs is 264,192 and 272,616 for Case 1 and Case 2, respectively. Considering the complexity of the cable architecture, the FE model size is low, achieved by using homogenization theory to reduce the axial length of the model and using beam elements for the armour layers.

5 Preliminary study

The are two main uncertainties in the model parameters: the friction coefficient and the radial pressure value, which are related to the surface interactions and initial stress state in the cable, respectively. To obtain a good agreement between numerical and experimental results, as in [28], the friction coefficient and pressure are adjusted on a a specific curvature range test. The Case 1 - pure stick IC contact interface, is considered in this section with a stick contact between the insulation and the conductors.

5.1 Influence of the friction coefficient on the global bending behaviour

To study the influence of the friction coefficient on the bending behaviour, the external pressure is fixed to 0.3 MPa. The friction coefficient values are chosen between 0 and 0.3. A cyclic loading with a curvature range of -0.05 m $^{-1}$ and 0.05 m $^{-1}$ is applied to the cable around the $\vec{y_1}$-axis. The bending cycle of the cable obtained from the numerical model is presented in Figure 13a.

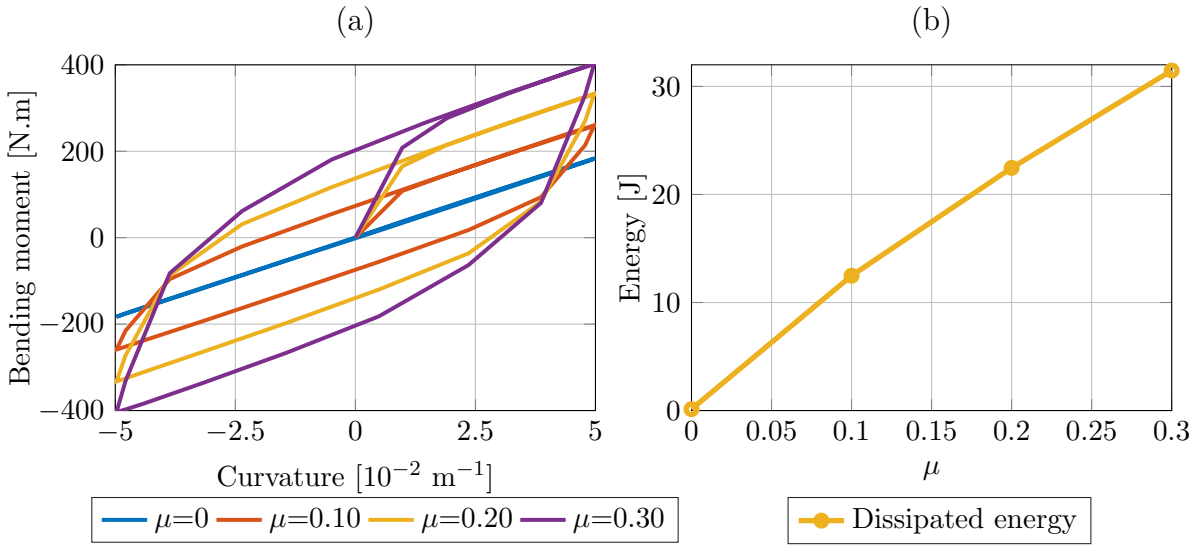

Figure 13: Evolution as a function of the friction coefficient of: the bending behaviour (a); the energy dissipated during the bending cycle (b)

When the friction coefficient $\mu = 0$, the cable components are free to slip, and the bending behaviour corresponds to the slip behaviour with minimal bending stiffness. However, for non-zero values of the friction coefficient, a non-linear bending behaviour is observed. At the first loading step, the bending stiffness is maximum, but it is important to note that the size of this loading step is such that slip occurs. The lower the coefficient of friction, the greater the slip, resulting in a lower stiffness than the stick stiffness, which is not dependent on the coefficient of friction. As curvature increases, the bending stiffness decreases until it reaches a minimum value, corresponding to the slip behaviour over the entire cross section. Figure 13a shows that this minimum bending stiffness is almost insensitive to the friction

coefficient, since the cable responses are parallel in the full slip zone. However, as the coefficient of friction increases, the tangential contact forces increase, resulting in a larger bending moment required to reach the full slip zone. This leads to increase the energy dissipated during the bending cycle, as shown in Figure 13b.

5.2 Influence of the external pressure on the global bending behaviour

As mentioned earlier, to introduce a normal contact force between the cable components, pressure is applied to the outer sheath of the numerical model. The influence of this pressure on the bending behaviour is analysed in this section, with the friction coefficient set at 0.2. The pressure values are varied between 0 MPa and 0.5 MPa., and a cyclic loading with curvature between -0.05 m $^{-1}$ and 0.05 m $^{-1}$ is applied to the cable around the $\vec{y_1}$-axis.

The bending behaviour obtained by the numerical model for different values of the pressure is presented in Figure 14. There is a strong similarity in the evolution of the cable response as a function of pressure and friction coefficient, as seen in Figures 14 and 13, respectively. For zero pressure, the cable is in a slip state as observed on Figure 13 for $\mu = 0$. In other words, even if friction is taken into account in the model, no normal contact force is present between the components before bending, so the cable components are free to slip. Increasing external pressure generates an increase in normal and frictional forces, which delays the transition to the full slip zone. As a result, the dissipated energy increases with pressure, as shown in Figure 14b. However, the external pressure has a little influence on the bending stiffness in the slip state.

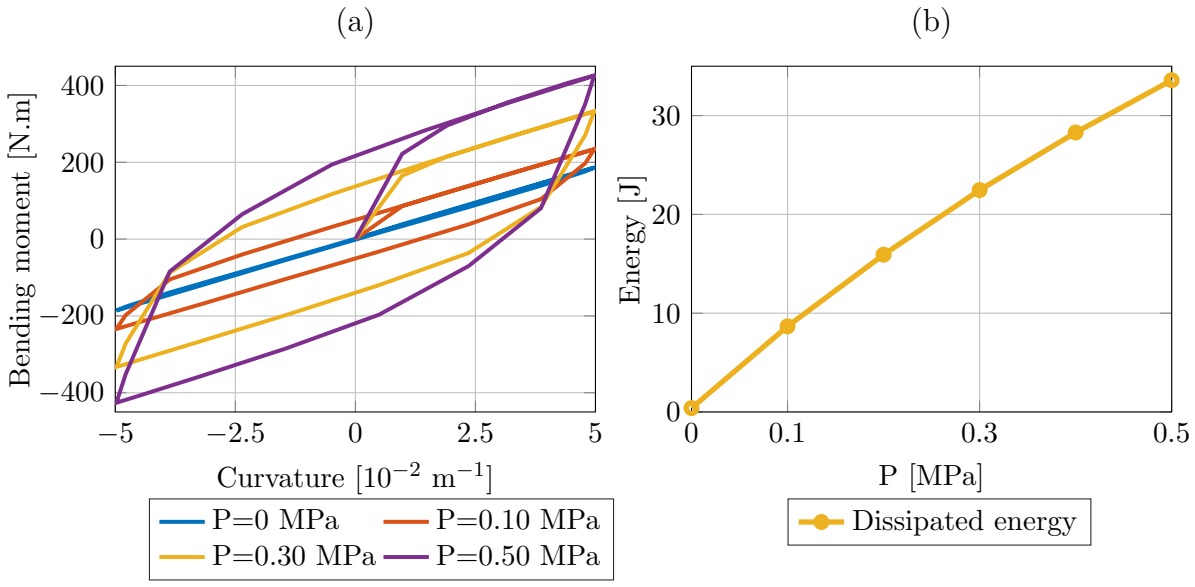

Figure 14: Evolution as a function of the external pressure of: the bending behaviour (a); the energy dissipated during the bending cycle (b)

5.3 Calibration of the numerical model on an experimental result

Calibrating the numerical model is akin to solving an equation with two unknowns: the friction coefficient and the external pressure. To simplify the problem, the friction coefficient

is set at 0.2, which is close to reference values in [3] and [34]. Therefore, the remaining parameter to consider is the external pressure, which is used to model the residual stresses.

To calibrate the numerical model with experimental results, two criteria are used: comparing the final bending stiffness obtained at the end of the loading and unloading steps, which coincides with the bending stiffness in the slip state, and comparing the energy dissipated during one bending cycle.

For this calibration, the load case considered is the same as the one in the two previous sections, namely a cyclic loading with a curvature of 0.05 m $^{-1}$ and 0.05 m $^{-1}$ around the $\vec{y_1}$-axis.

Figure 15a shows a comparison between numerical model and experimental tests. For each external pressure value, the relative deviation between the numerical model and the test is calculated for the bending stiffness at the end of loading and unloading steps, as well as for the energy dissipated during the bending cycle, see Figures 15b and 15c, respectively. Figure 15b shows that the stiffness obtained by the numerical model is very close to the bending stiffness of the test, with a maximum relative deviation of 7.50 %. However, there is a significant difference in terms of dissipated energy in Figures 15a and 15c when the external pressure deviates from 0.3 MPa.

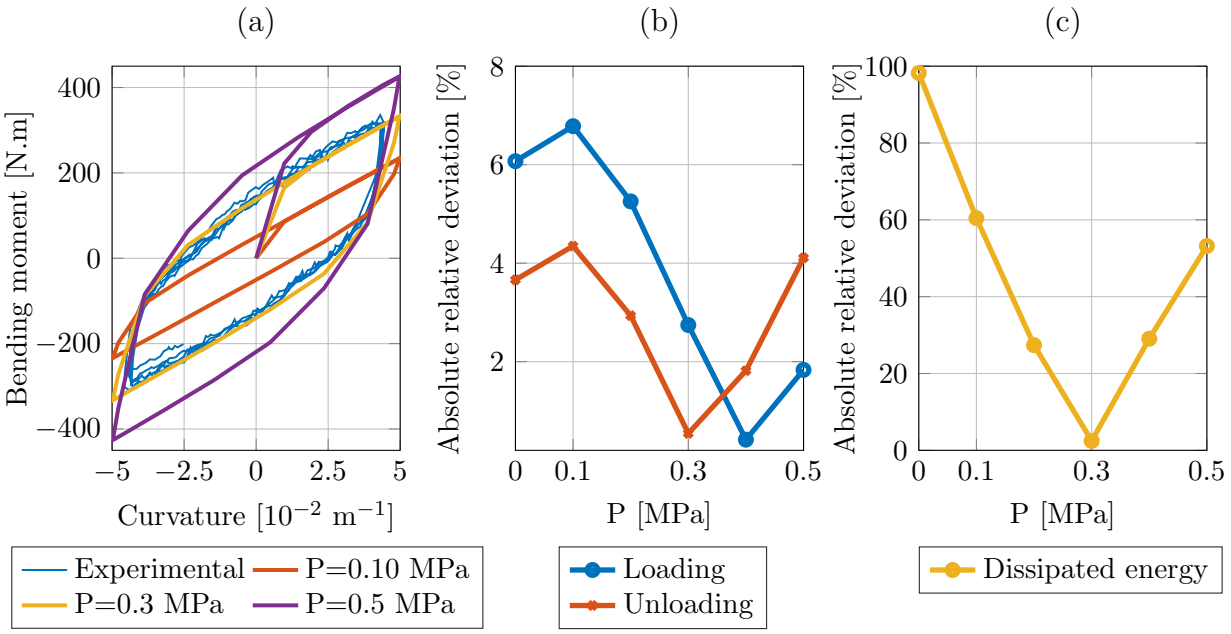

Figure 15: Evolution as a function of the external pressure of: the bending behaviour (a); the absolute relative deviation between the numerical stiffness and the test stiffness at the end of loading and unloading steps (b); the absolute relative deviation between the numerical model and the test in terms of energy dissipated during the bending cycle (c)

It appears that with a friction coefficient $\mu = 0.2$, the pressure value of 0.3 MPa better reproduces the test results. These two parameters are then fixed in the following section for the modelling of each experimental loading case, in order to compare the numerical results

to experimental values.

6 Global and local analysis from numerical results

The numerical model is used to study both the overall bending stiffness of the cable and local quantities, including stresses in conductor, displacements of the components and contact forces.

6.1 Comparison of the bending behaviour between numerical, experimental and analytical results

Figure 16 displays the bending moment-curvature diagram obtained from the tests and the numerical model with Case 1 - pure stick IC contact interface between the insulation and the conductors for various curvature ranges. For comparison purposes, the minimum bending moment obtained from the analytical solution [20], see Appendix A, is shown for each load case. Figures 16a and 16b depict a bending cycle centred on zero while Figures 16c to 16f correspond to a bending cycle starting at zero. For each load case, the solution is obtained with a computational time of approximately 1 hour with 4 cores Intel Xeon (Haswell) having 5.33 Gb of memory per core.

The length of the test bench is 2.5 m, while the length with constant bending moment is 1.25 m. On the other hand, the pitch lengths of the outer armour layer, inner armour layer and power core are 0.73 m, 0.64 m and 0.70 m, respectively. Thus, end effects might have an influence on the tests results. However, this has not been investigated in this work since only one type of cable has been tested and it was not feasible to modify the test bench.

A very good agreement is observed among numerical, experimental and analytical values. For each test, the non-linear behaviour is well predicted by the numerical model.

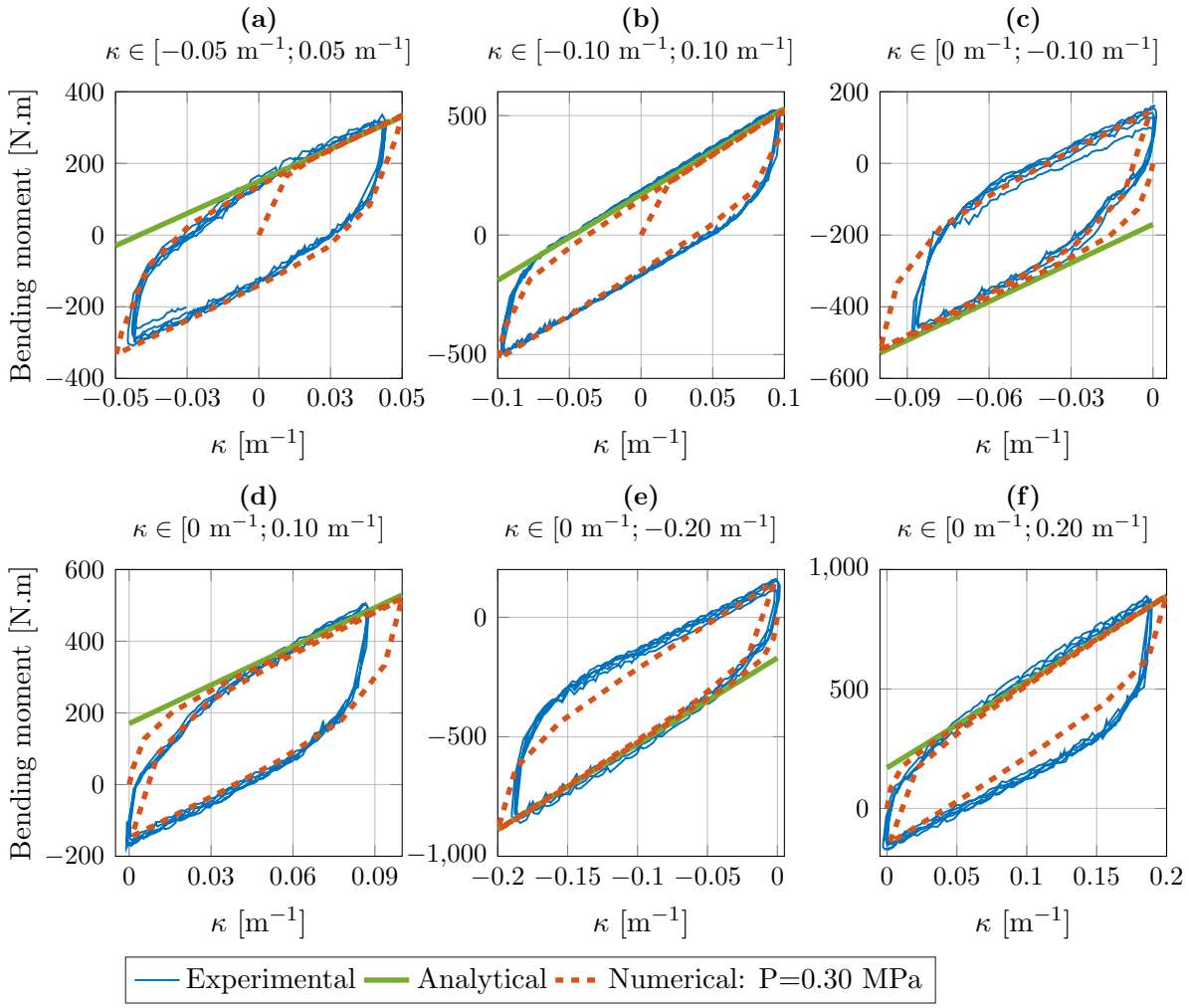

Figure 16: Comparison of the bending moment-curvature diagram between numerical, experimental and analytical [20] results for bending cycles with different curvature ranges

Table 3 displays the minimum bending stiffness in the slip zone at the end of loading and unloading steps. For a given curvature range, the values obtained from numerical model are close, while this is not the not always the case for the tests results, which may be attributed to residual stresses from storage. This is more pronounced for a curvature of 0.2 m $^{-1}$, resulting in an increase in the difference between the numerical and test bending stiffness.

As the curvature increases, the bending stiffness obtained by the numerical model and tests tend to approach the minimum stiffness value given by the analytical solution. However, friction between the components after slip leads to a difference between the minimum analytical stiffness corresponding to a full slip behaviour and the stiffness obtained in the numerical simulations and tests.

In terms of energy dissipated during the bending cycle, small differences between the numerical model and the tests are observed, with a maximum relative deviation of less than 8%. The target curvature ranges in the numerical simulation are the ranges defined in section

3.5, whereas the experimental curvature ranges sometimes differ from these target values. This discrepancy leads to an artificial increase in the difference between the numerical and experimental results. During the tests, step increments of bending force are applied until the sample displacement measured at the midpoint approaches the deflection corresponding to the curvature target value. After the tests, the curvature was computed more accurately from the three measurements of sensors located between the two actuators, as described in sections 3.2 and 3.3, revealing a discrepancy with the previous value calculated only from the midpoint sensor. This explains the difference between experimental and targeted curvature ranges, which is the main source of error in energy dissipated between numerical model and tests. Moreover, as shown in sections 5.1 and 5.2, the numerical model underestimates the bending stiffness at the beginning of the loading, which also accounts for this difference.

Curvature $[m^{-1}]$	**Model**	**Minimum stiffness loading** $[N.m^2]$	**Minimum stiffness unloading** $[N.m^2]$	**Dissipated energy** $[J]$
[-0.05;0.05] Figure 16a	test	3955	3854	21.92
	numerical	3846	3834	22.46
	relative deviation [%]	2.74	0.54	-2.46
[-0.10;0.10] Figure 16b	test	3529	3410	61.60
	numerical	3701	3700	57.20
	relative deviation [%]	-4.87	-8.49	7.14
[0;-0.10] Figure 16c	test	3517	3990	21.41
	numerical	3807	3795	22.11
	relative deviation [%]	-8.24	4.90	-3.27
[0;0.10] Figure 16d	test	3943	3615	21.27
	numerical	3807	3796	22.11
	relative deviation [%]	1.71	-4.99	-3.45
[0;-0.20] Figure 16e	test	3296	3554	52.25
	numerical	3696	3623	50.03
	relative deviation [%]	-12.16	-1.93	4.25
[0;0.20] Figure 16f	test	3677	3083	52.98
	numerical	3697	3623	52.63
	relative deviation [%]	-0.53	-17.51	5.57
All loading case	Analytical minimum bending stiffness	3593	3593	-

Table 3: Comparison of the minimum stiffness values at the end of the loading and unloading steps and of the dissipated energy between the test results and the numerical and analytical results

6.2 Axial stress prediction from analytical model

Analytical models provide axial stress expressions within the helical component such as conductors, which are one of the most fatigue-sensitive parts of the cable. The conductors are approximated as continuous cylinders with a helical mean line. The analytical solution presented in this study is obtained with the following assumptions:

- all components have linear elastic behaviour,
- helical components slide along a loxodromic path,

- radial contact in the same layer is neglected,
- the cable is bent to a constant curvature κ,
- the cross-section deformation of the cable during bending is not considered.

The axial stress σ_{33}, which is defined in the cable axial direction, is decomposed into three components: σ_A induced by axisymmetric loads (tension-torsion and radial pressure), σ_B due to the local change of the component curvature and σ_f generated by the frictional interaction between components:

$$\sigma_{33} = \sigma_A + \sigma_B + \sigma_f. \tag{13}$$

The first term σ_A is generally given by axisymmetric analysis from analytical or numerical models such as in [8] and [9].

According to [45], the local bending stresses σ_B can be obtained by:

$$\sigma_B = E\left[X_2 cos\alpha(1 + sin^2\alpha)cos\theta + X_3 cos^2\alpha cos2\alpha sin\theta\right]\kappa, \tag{14}$$

where E is the Young's Modulus, θ is the angular position of the component in the cross-section and α is its lay angle. Variables X_2 and X_3 are the local coordinates in the component, as shown in Figure 17a for a curvature around the $\vec{y_1}$-axis.

At the beginning of the slip phase, the critical curvature κ_c (see [21]) can be defined by:

$$\kappa_c = \frac{f}{EAcos^2\alpha sin\alpha}\frac{\theta}{sin\theta}, \tag{15}$$

where A is the cross-sectional area of the component and f the frictional force per unit length acting on the component boundary.

As reported by [21] and [34], if the contact between components in the same layer is neglected, the frictional force can be determined by the following expression:

$$f = \mu_i q_i + \mu_0 q_0, \tag{16}$$

in which μ_i and μ_0 are the friction coefficients of the adjacent inner and the outer layers, respectively, and q_i and q_0 are the contact force per unit of length along the contact line of the inner and outer helices, respectively. At the beginning of the slip phase, the frictional force induces axial stress σ_f given by:

$$\sigma_f = \frac{R_h\theta}{Asin\alpha}f, \quad \text{with } \theta \in [-\pi/2; \pi/2], \tag{17}$$

the frictional force being symmetric with respect to $\vec{y_2}$-axis.The frictional force is usually obtained from an axisymmetric analysis with analytical or FE models. In this work, it is determined from the results of the 3D FE model.

A graphical evolution of axial stress in a helical component during a stick-slip behaviour is shown in Figure 17b. The bending behaviour consists of two linear approximations. The

stick zone is defined between the axial stress coordinates ($\kappa = 0$; σ_A) and the frictional stress coordinates ($\kappa = \kappa_c$; $\sigma_A + \sigma_f$). Then, the slip zone starts with a slope of $\frac{\sigma_B}{\kappa}$.

In the case of a loxodromic assumption, the axial displacement u_3 of a component is given by the following equation [34]:

$$u_3 = R_h^2 \frac{cos^2\alpha}{sin\alpha} \kappa cos\theta. \tag{18}$$

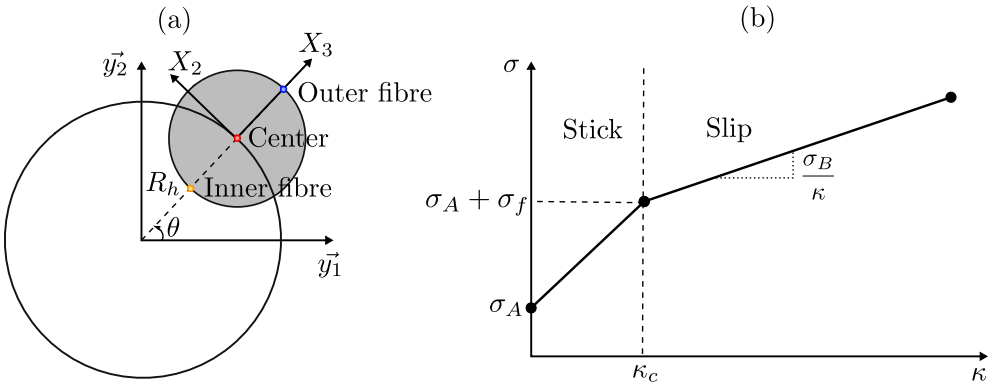

Figure 17: Local coordinates within an helical component (a) and representation of the stick-slip behaviour (b)

6.3 Local displacement

Figure 18a shows the transverse deflection at one end cross-section of the model for the maximum curvature of 0.2 m^{-1} around the $\vec{y_1}$-axis. For this loading case, the maximum displacement is 1.26 mm which corresponds to 1.25% of the cable cross-section diameter. Therefore, the small displacements assumption is valid for curvatures equal to or less than 0.2 m^{-1}.

The axial displacement of the inner armour layer obtained by the numerical model is shown in Figure 18b for curvatures from 0.05 m^{-1} to 0.02 m^{-1}. For each curvature, it can be observed that the armour layer displacement is close to the displacement predicted by a loxodromic curve given by the equation (18). This observation also applies to the conductors and the insulation, as shown in Figure 18c, in Case 1 - pure stick IC contact interface or Case 2 - frictional IC contact interface.

When the conductor is bonded to the insulation, no relative displacement is allowed. Thus, the slip mechanism is controlled by the friction around the boundary of the power core. In Case 2 - frictional IC contact interface, some relative displacements occur between the insulation and the conductors, as shown in Figure 19. As predicted by the equation (18), these relative displacements are equal to zero when the angle with respect to the bending axis is $\pm\pi/2$. For other angular positions, some relative displacement appear between the core and the inner sheath and also between the insulation and the conductor. It can be observed that when the core is in a stick state ($\kappa \leq 0.02$ m^{-1} for example), the conductor seems to

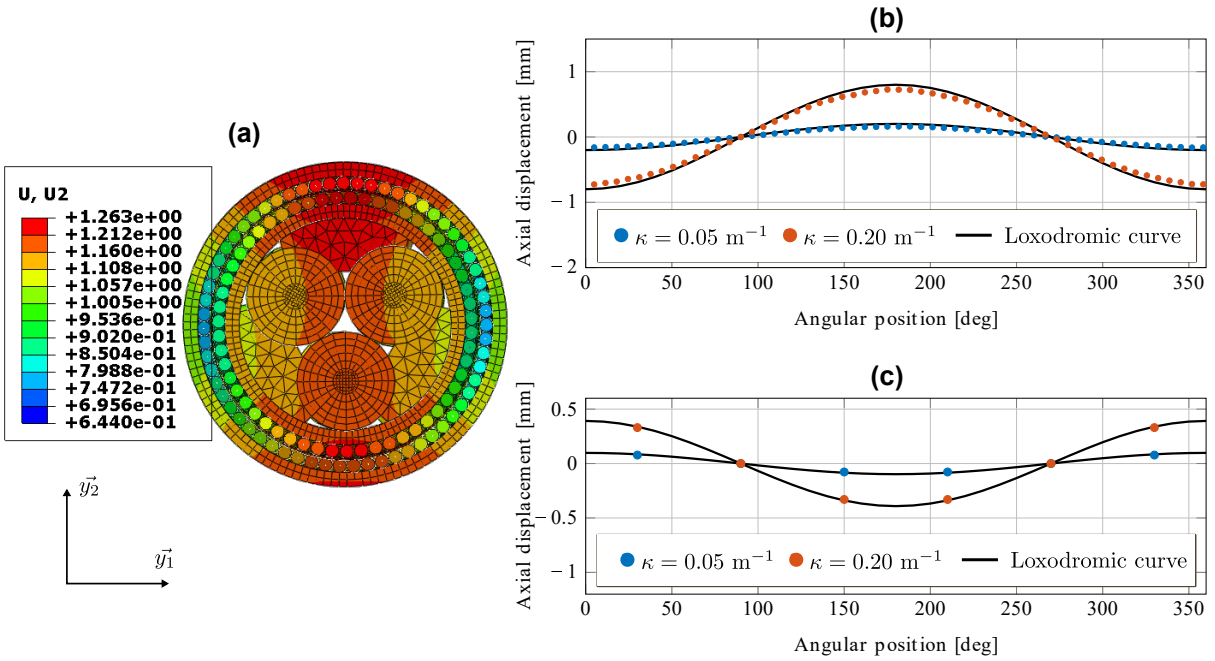

Figure 18: Deflection distribution at one end of the model at 0.2 m^{-1} around $\vec{y_1}$-axis (a); axial displacement between inner armour layer and the inner sheath for 0.05 m^{-1} and 0.2 m^{-1} (b); axial displacement between the core and the inner sheath for 0.05 m^{-1} and 0.2 m^{-1} (c)

slip into the insulation. And when the core is in a slip state (0.02 m^{-1} $< \kappa \leq$ 0.05 m^{-1} for example), the slip between the conductor and the insulation remains almost constant as the curvature increases.

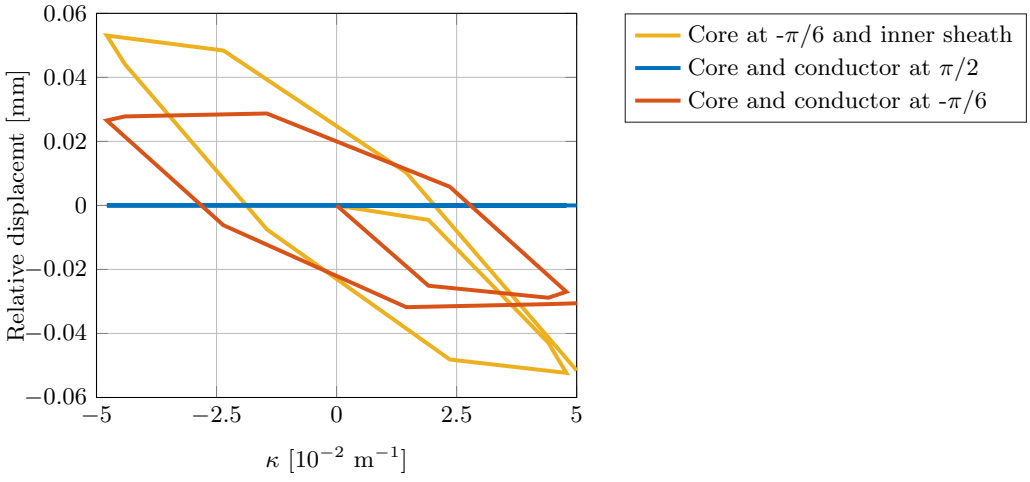

Figure 19: Relative displacement between the conductors and the insulation during a cyclic loading $\kappa \in [-0.05\ \text{m}^{-1}; -0.05\ \text{m}^{-1}]$

6.4 Contact force transmission between layers

Figure 20 presents the distribution of the contact force between the inner sheath and the cores and fillers at the end of the radial pressure step: P=0.3 MPa. As with simple metallic strand [38], the distribution of this contact force strongly depends on the position of the contact point between the outer and the inner armour layers. When two wires belonging to two different layers are at the same angular position, the transmission of the contact force is maximum, even if there is a thin sheath between the layers. Conversely, the transmission is minimum if the difference in angular position is maximum, as shown in Figure 21. This phenomenon causes a sinusoidal distribution of the contact lineload in the normal direction. For instance, Figure 20b shows that the lineload between the cores and the inner sheath oscillates around a mean value of 1.9KN/m.

Figure 20c reveals that the mean lineload acting on the whole surface of the internal sheath remains almost constant throughout the bending cycle, with a value close to 46KN/m. Similarly, by integrating the contact forces around the contact surface of a core, one can obtain the mean lineload applied to a core, which is also almost constant during the bending cycle with a value close to 16.5 KN/m. This result is consistent with that of [34] for a power cable with three cores, where the inner sheath transmits about 1/3 of the lineload to each core. In Case 2 - frictional IC contact interface, assuming frictional contact between the insulation and the conductors, the mean lineload acting on conductor is also constant during the bending cycle with a value close to 4,3 KN/m. These lineload values will be used in the following in the analytical model to predict the stress evolution within the conductor during the bending cycle with the two contact assumptions: Case 1 - pure stick IC contact interface or Case 2 - frictional IC contact interface - between the insulation and the conductors.

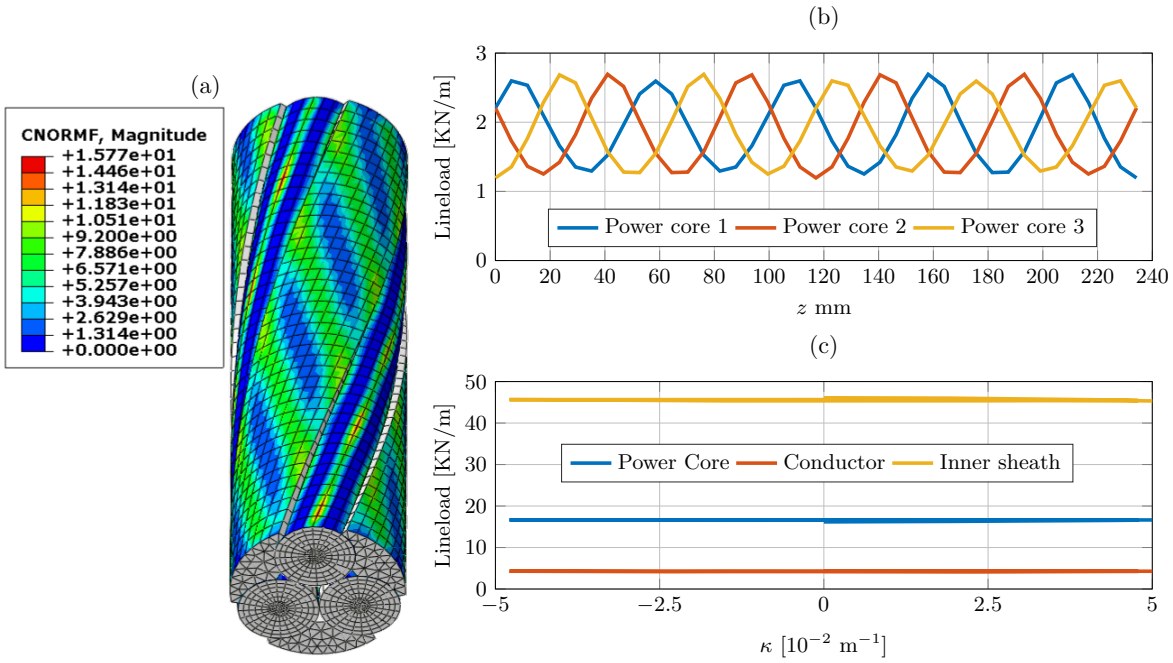

Figure 20: Normal contact force distribution over the fillers and power cores at the end of the radial pressure step: P=0.3 MPa (a); lineload distribution along axial position acting on power cores at $\kappa = 0\text{m}^{-1}$(b); mean lineload evolution acting on one power core and on the inner sheath for $\kappa \in [-0.05\ \text{m}^{-1}; 0.05\ \text{m}^{-1}]$

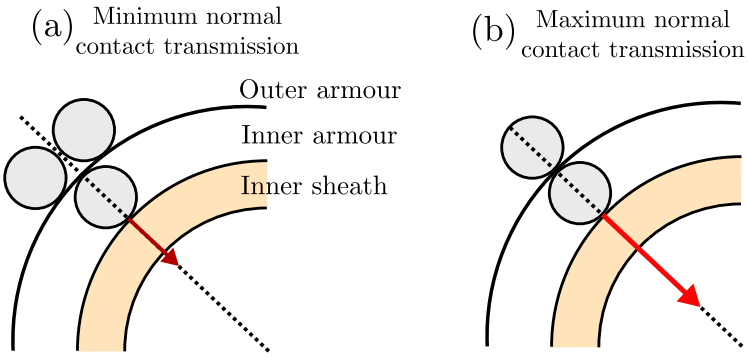

Figure 21: Representation of the contact normal force transmission between armour layers: without (a) and with (b) radial alignment of the wires

6.5 Local axial stress analysis in the conductor

To study the fatigue strength of the cable, quantities of interest are the local stresses, especially the axial stresses in the conductors, obtained by the FE model for the two contact assumptions: Case 1 - pure stick IC contact interface or Case 2 - frictional IC contact interface - between the insulation and the conductors. The numerical results are compared with the analytical results resulting from the equations (13) to (17). The loading case under study is a cyclic bending with curvature between 0.05 m $^{-1}$ and 0.05 m $^{-1}$ around the $\vec{y_1}$-axis with an initial pressure of 0.3 MPa.

The axial stresses are computed for different core positions in the cable cross-section. In the case of bending around the $\vec{y_1}$-axis, the axial stress is maximum when one core is at the angular position of $\theta = \pi/2$, as shown in Figure 22a and the minimum is obtained at an angular position of $\theta = -\pi/2$, as shown in Figure 22b for the Case 1 - pure stick IC contact interface. For these two angular positions the friction stress is actually maximum, as shown by equation (17). The maximum or minimum axial stresses are reached at the node furthest from the bending axis, i.e., on the outer fibre of the conductor. The axial stresses are close to zero when the angular position of the conductor corresponds to the bending axis, for which the friction stress is zero. The stress distribution for the Case 2 - frictional IC contact interface is similar to that of the Case 1 - pure stick IC contact interface, but with lower extremum values than in Case 1, as shown in the following.

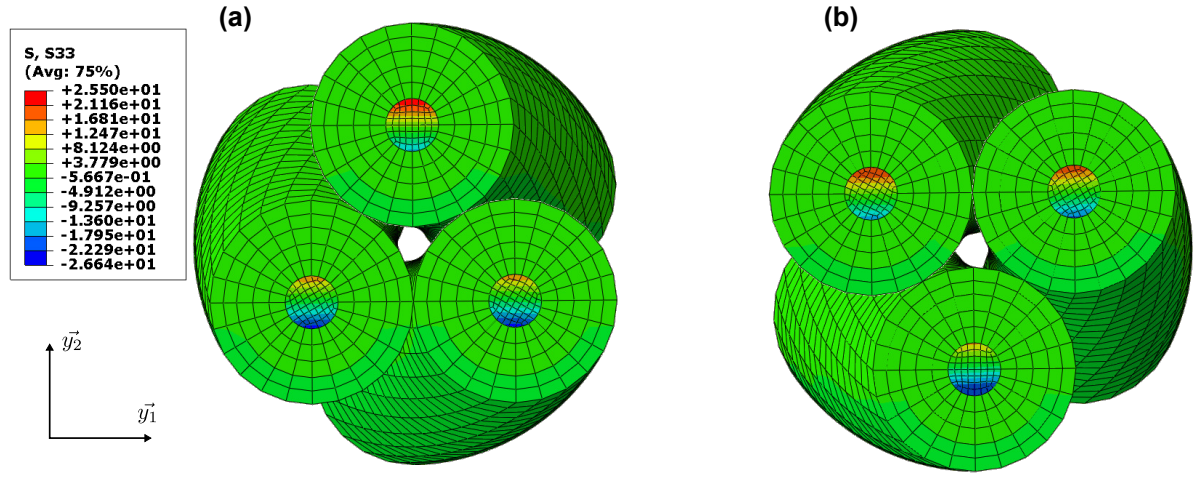

Figure 22: Axial stress distribution in the cores for the Case 1 - pure stick IC contact interface and $\kappa = 0.05$ m^{-1}: core at $\theta = \pi/2$ (a) and core at $\theta = -\pi/2$ (b)

Figure 23 shows the evolution of the numerical and analytical axial stresses in the conductor for the Case 1 - pure stick IC contact interface for $\theta = \pi/2$ and $\theta = -\pi/6$. In Figure 24, the axial stress evolution is presented for the Case 2 - frictional IC contact interface. In both cases, almost zero axial stress is generated by the application of an external pressure before the bending cycle. Therefore, σ_A is assumed to be zero in the analytical model, as seen in Eq (13).

An overall stick-slip behaviour is obtained, regardless the contact assumption between the insulation and the conductor. The maximum and minimum stresses occur for an angular position of $\theta = \pm\pi/2$, where the frictional stress and the distance to bending axis are maximum, unlike the angular position $\theta = -\pi/6$. It can be seen that the stresses for the Case 1 - pure stick IC contact interface model are close to those of the Case 2 - frictional IC contact interface. The main differences between the two models are in the stiffness in the stick zone, which is logically larger for the stick contact interface, leading to a larger dissipated energy during one bending cycle.

It can also be observed from Figures 23 and 24 a good level of agreement between the FE

simulations and analytical model. However, it is important to point out some limitations of the analytical model, explaining the discrepancy with numerical results. The most significant discrepancies occur in the stick zone for both models. In the analytical model, the full stick assumption is made over the whole cross-section, whereas small slips are present in the numerical models, decreasing the cable stiffness. In contrast, there is a very good agreement between the numerical and analytical results for the stiffness in the slip zone. Additionally, the analytical model is based on a configuration consisting of a layer of components, in contact with a central core, as shown in Figure 17, assuming no radial contact in the layer. However, in the case of three cores, there is no central core, but a radial contact exists between the three cores. Moreover, in the Case 1 - pure stick IC contact interface model, a relative slip between the three cores is observed in the numerical model, leading to the stick-to-slip transition at lower stresses than the analytical model. This may be the source of the conservatism of the analytical model, as reported in [34].

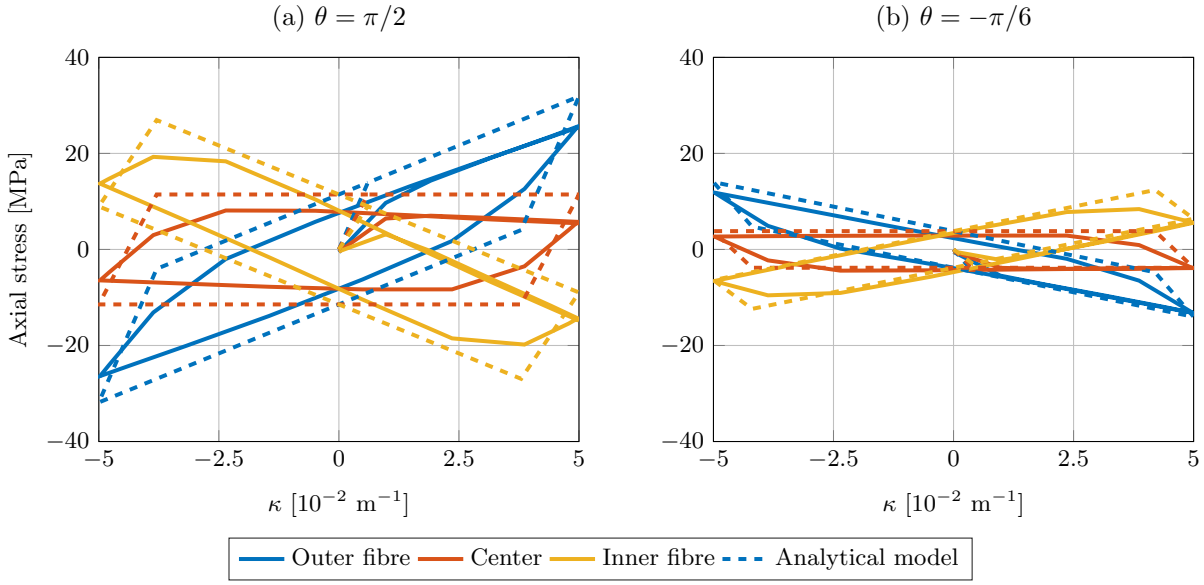

Figure 23: Axial stress in the conductor for the Case 1 - pure stick IC contact interface and $\kappa \in [-0.05\ \text{m}^{-1}$; $0.05\ \text{m}^{-1}]$ at $\theta = \pi/2$ (a) and $\theta = -\pi/6$ (b)

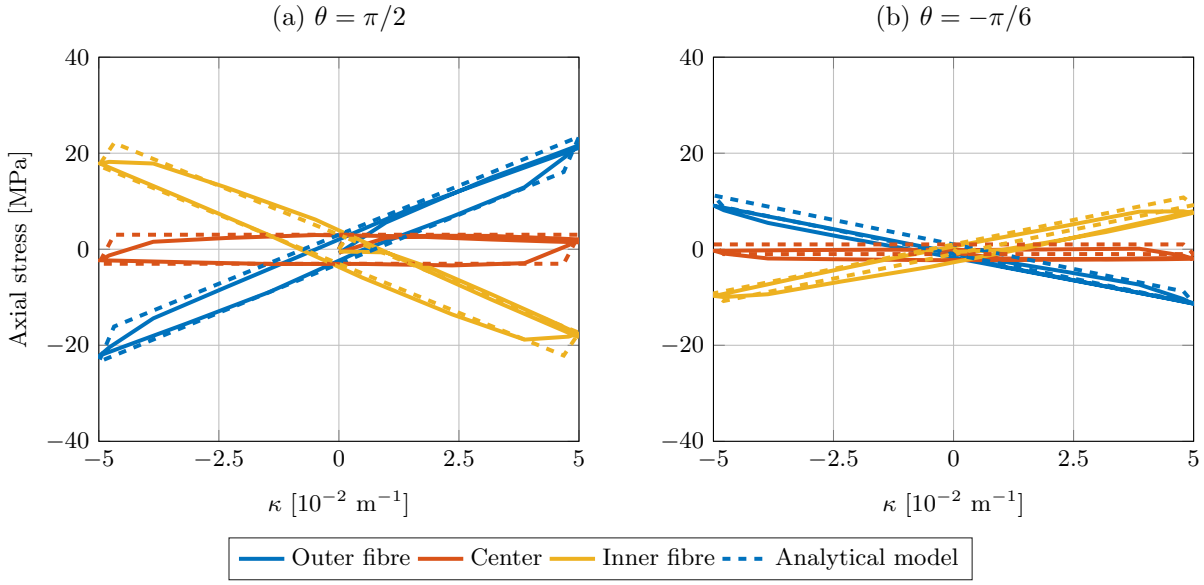

Figure 24: Axial stress in the conductor for the Case 2 - frictional IC contact interface and $\kappa \in [-0.05\ \text{m}^{-1}$; $0.05\ \text{m}^{-1}]$ at $\theta = \pi/2$ (a) and $\theta = -\pi/6$ (b)

7 Conclusion

This paper presents a computationally efficient approach based on a 3D local FE model for simulating the global mechanical behaviour and for calculating the local stress state of dynamic submarine power cables. The method is applied to a three core cable subjected to cyclic bending loading with curvature ranges representative of the cable service state. The numerical approach is based on the homogenization theory of periodic structures, which allows to define a problem posed on a helical period of the cable internal components. In addition, beam elements are used to model the armour layers, which further reduces the size of the computational domain. Thus, the model can accurately account for the geometrical complexity and contact interactions between the cable's internal components.

A series of experimental tests are performed on a three core cable. The geometrical data of this cable are known and material parameters are taken from material databases or other studies dedicated to dynamic submarine power cables. However, some input data are not available in the numerical model, such as friction coefficients and initial stress state due to the cable manufacturing process. One test is used to calibrate the missing input data. The numerical results are compared to experimental values, such as the bending stiffness in the slip state and the dissipated energy during the bending cycle. The results show that the friction coefficient has a significant impact on the overall bending behaviour in the stick state, while it has a weak influence in the slip state. Moreover, the radial pressure representing the initial stress state generates a non-zero normal contact force, affecting the bending stiffness in the stick state and to the stick-to-slip transition. The pressure value is calibrated on one test, and the calibrated model shows overall bending stiffness values that closely match the results of the other tests.

A validation of the local solutions is performed by comparing the FE results with the predictions of analytical models in the literature. The longitudinal displacement, contact force and axial stress are analysed. The longitudinal displacement of the helical components such as armour layers and cores agrees well with the analytical loxodromic curve. The distribution of the contact force along the axial direction of the cable depends on the distribution of the contact point between the armour layers, leading to a sinusoidal contact transmission. Furthermore, it is observed that the mean contact lineload between the components remains constant during the bending load cycle. The evolution of the axial stress in the conductor obtained from numerical model is in good agreement with the prediction of the analytical model. However, it should be noted that the analytical model requires the value of the contact force, which is obtained from the FE model results. Additionally, the FE model provides more details at the local scale, particularly in terms of component compliance and slip phenomena, which create a smaller axial stress range than the analytical model. In the case of a cable without a central core, the analytical model needs to be improved to take into account the evolution of contact and frictional stresses between the three cores.

8 Acknowledgments

This work has received support from France Energies Marines, along with State subsidies managed by the National Research Agency, as part of the Investments for the Future program, under the reference ANR-10-IEED-0006-28.

Appendix A Minimum bending moment of the dynamic cable from analytical solution

This appendix presents the equations for calculating the minimum bending moment of a dynamic cable with three cores, which are taken from [20]. The minimum bending moment is influenced by the geometry of each component. The components can be classified into three types based on their geometry: helical components with a circular cross-section (amours and cores), helical components with a,non-circular section (fillers) and straight cylindrical components (outer and inner sheath).

When the slip state is reached, the minimum contribution to the bending moment of a helical layer i composed of $n_{w,i}$ components with circular cross-section can be written as follows:

$$M_{w,i} = \frac{1}{2} n_{w,i} (EI^n_{w,i} + EI^b_{w,i} cos^2 \alpha_{w,i}) \kappa, \tag{A.1}$$

where $EI^n_{w,i}$ et $EI^b_{w,i}$ are the bending stiffness in the normal and bi-normal direction to the component mean-line, respectively.

In the particular case of fillers, the cross-section of the component is non-circular and the local twist is taken into account. Thus, the minimum bending moment of a layer i of $n_{f,i}$ fillers is determined by:

$$M_{f,i} = \frac{1}{2} n_{f,i} (EI^n_{f,i} + EI^y_{f,i} cos^2 \alpha_{f,i} + GJ_{f,i} sin^2 \alpha_{f,i}) \kappa, \tag{A.2}$$

where $EI^n_{f,i}$, $EI^b_{f,i}$ and $GJ_{f,i}$ are the bending stiffness in the normal and bi-normal direction to the component mean-line and the component torsional stiffness, respectively.

The resultant bending moment from the cylindrical layers i can be determined by the following equation:

$$M_{c,i} = EI_{c,i}\kappa, \tag{A.3}$$

with $EI_{c,i}$ the bending stiffness of the component.

Therefore, considering the geometry of all components of the dynamic cable, the minimum bending moment M_{min} of the dynamic cable can be expressed as follows:

$$M_{min} = \sum_{i=1}^{m_1} M_{w,i} + \sum_{i=1}^{m_2} M_{f,i} + \sum_{i=1}^{m_3} M_{s,i}, \tag{A.4}$$

where m_1, m_2 and m_3 are the number of helical layers of component with circular cross-section, non-circular cross-section and the number of straight cylindrical components, respectively.

References

[1] G. P. Drumond, I. P. Pasqualino, B. C. Pinheiro, S. F. Estefen, Pipelines, risers and umbilicals failures: A literature review, Ocean Engineering 148 (2018) 412–425.

[2] P. R. Thies, L. Johanning, G. H. Smith, Assessing mechanical loading regimes and fatigue life of marine power cables in marine energy applications, Proceedings of the Institution of Mechanical Engineers, Part O: Journal of Risk and Reliability 226 (2012) 18–32.

[3] J.-M. Leroy, F. Caleyron, Y. Poirette, N. B. Dupend, Assessing Mechanical Stresses in Dynamic Power Cables for Floating Offshore Wind Farms, Proceedings of the ASME 2017 36th International Conference on Ocean, Offshore and Arctic Engineering, Trondheim, Norway (2017).

[4] S.-H. Yang, J. W. Ringsberg, E. Johnson, Parametric study of the dynamic motions and mechanical characteristics of power cables for wave energy converters, Journal of Marine Science and Technology 23 (2018) 10–29.

[5] D. G. Young, C. Ng, S. Oterkus, Q. Li, L. Johanning, Assessing the mechanical stresses of dynamic cables for floating offshore wind applications, Journal of Physics: Conference Series 1102 (2018) 012016.

[6] L. Okkerstrøm, O. T. Gudmestad, E. Pedersen, Simulation of peak tension loads in subsea power cables during installation, IOP Conference Series: Materials Science and Engineering 1201 (2021) 012010.

[7] J. Witz, Z. Tan, On the axial-torsional structural behaviour of flexible pipes, umbilicals and marine cables, Marine Structures 5 (1992) 205–227.

[8] A. Custódio, M. Vaz, A nonlinear formulation for the axisymmetric response of umbilical cables and flexible pipes, Applied Ocean Research 24 (2002) 21–29.

[9] S. Sævik, S. Bruaseth, Theoretical and experimental studies of the axisymmetric behaviour of complex umbilical cross-sections, Applied Ocean Research 27 (2005) 97–106.

[10] Y. Bai, Y. Lu, P. Cheng, Analytical prediction of umbilical behavior under combined tension and internal pressure, Ocean Engineering 109 (2015) 135–144.

[11] H.-C. Chang, B.-F. Chen, Mechanical behavior of submarine cable under coupled tension, torsion and compressive loads, Ocean Engineering 189 (2019) 106272.

[12] P. Fang, X. Jiang, H. Hopman, Y. Bai, Mechanical responses of submarine power cables subject to axisymmetric loadings, Ocean Engineering 239 (2021) 109847.

[13] S. Ehlers, M. Biglu, F. von Bock und Polach, W. Thießen, Experimental and numerical investigations of the ultimate strength of two subsea power-transmission cables, Marine Structures 88 (2023) 103346.

[14] P. Maioli, Bending stiffness of submarine cables, International Conference on Insulated Power Cables, Versailles, France (2015).
[15] T. Ottesen, Experimental Investigation of Power Umbilical Damping, Proceedings of the ASME 2017 36th International Conference on Ocean, Offshore and Arctic Engineering, Trondheim, Norway (2017).
[16] R. Knapp, M. Cruickelan, Design methodology for undersea umbilical cables, Ocean Technologies and Opportunities in the Pacific for the 90's (1991) 1319–1327.
[17] R. Knapp, Axial fatigue model for wire rope strand, Proc. ASCE 1987 Structures Congress (1979) 347–359.
[18] K. Papailiou, On the bending stiffness of transmission line conductors, IEEE Transactions on Power Delivery (1997) 1576–1588.
[19] G. Costello, Theory of wire rope, Springer-Verlag, 2nd edition, 1997.
[20] J. Witz, Z. Tan, On the flexural structural behaviour of flexible pipes, umbilicals and marine cables, Marine Structures 5 (1992) 229–249.
[21] G. Skeie, N. Sødahl, O. Steinkjer, Efficient Fatigue Analysis of Helix Elements in Umbilicals and Flexible Risers: Theory and Applications, Journal of Applied Mathematics 2012 (2012) 1–22.
[22] J. J. Feŕet, C. L. Bournazel, Calculation of Stresses and Slip in Structural Layers of Unbonded Flexible Pipes, Journal of Offshore Mechanics and Arctic Engineering 109 (1987) 263–269.
[23] S. Sævik, On Stresses and Fatigue in Flexible Pipes, Ph.D. thesis, Norwegian Institute of Technology, Trondheim, Norway, 1992.
[24] I. Kraincanic, E. Kebadze, Slip initiation and progression in helical armouring layers of unbonded flexible pipes and its effect on pipe bending behaviour, The Journal of Strain Analysis for Engineering Design 36 (2001) 265–275.
[25] Q. Lu, Z. Yang, J. Yan, H. Lu, J. Chen, Q. Yue, A Finite Element Model for Prediction of the Bending Stress of Umbilicals, Journal of Offshore Mechanics and Arctic Engineering 139 (2017).
[26] S. Sævik, K. I. Ekeberg, Non-Linear Stress Analysis of Complex Umbilical Cross-Sections, 21st International Conference on Offshore Mechanics and Arctic Engineering, Volume 1 (2002) 211–217.
[27] F. P. Nasution, S. Sævik, S. Berge, Experimental and finite element analysis of fatigue strength for 300 mm2 copper power conductor, Marine Structures 39 (2014) 225–254.
[28] H. Hu, J. Yan, S. Sævik, N. Ye, Q. Lu, Y. Bu, Nonlinear bending behavior of a multilayer copper conductor in a dynamic power cable, Ocean Engineering 250 (2022) 110831.
[29] D. Zhang, M. Ostoja-Starzewski, Finite Element Solutions to the Bending Stiffness of a Single-Layered Helically Wound Cable With Internal Friction, Journal of Applied Mechanics 83 (2016) 031003.
[30] W.-G. Jiang, A concise finite element model for pure bending analysis of simple wire strand, International Journal of Mechanical Sciences 54 (2012) 69–73.
[31] I. Probyn, A. Dobson, M. Martinez, Advances in 3d fea techniques for metallic tube umbilicals, ISOPE, Lisbon, Portugal (2007).
[32] V. Le Corre, I. Probyn, Validation of a 3-Dimensional Finite Element Analysis Model of Deep Water Steel Tube Umbilical in Combined Tension and Cyclic Bending, Volume 3: Pipeline and Riser Technology (2009) 77–86.
[33] F. Caleyron, M. Guiton, J. Leroy, T. Perdrizet, D. Charliac, P. Estrier, L. Paumier, A Multi-Purpose Finite Element Model for Flexible Risers Studies, Volume 6A: Pipeline and Riser Technology (2014).
[34] D. D. Tjahjanto, A. Tyrberg, J. Mullins, Bending Mechanics of Cable Cores and Fillers in a Dynamic Submarine Cable, International Conference on Ocean, Offshore and Arctic Engineering (2017).
[35] T. V. Lukassen, E. Gunnarsson, S. Krenk, K. Glejbøl, A. Lyckegaard, C. Berggreen, Tension-bending analysis of flexible pipe by a repeated unit cell finite element model, Marine Structures 64 (2019) 401–420.
[36] A. Kolpakov, Calculation of the characteristics of thin elastic rods with a periodic structure, Journal of Applied Mathematics and Mechanics 55 (1991) 358–365.
[37] P. Cartraud, T. Messager, Computational homogenization of periodic beam-like structures, International Journal of Solids and Structures 43 (2006) 686–696.
[38] F. Ménard, P. Cartraud, Solid and 3d beam finite element models for the nonlinear elastic analysis of

helical strands within a computational homogenization framework, Computers & Structures 257 (2021) 106675.
[39] M. A. Saadat, D. Durville, A mixed stress-strain driven computational homogenization of spiral strands, Computers & Structures 279 (2023) 106981.
[40] N. Buannic, P. Cartraud, Higher-order effective modeling of periodic heterogeneous beams. I. Asymptotic expansion method, International Journal of Solids and Structures (2001) 23.
[41] J.-S. Kim, M. Cho, E. C. Smith, An asymptotic analysis of composite beams with kinematically corrected end effects, International Journal of Solids and Structures 45 (2008) 1954–1977.
[42] R. Baumann, P. Novak, Efficient computation and experimental validation of ACSR overhead line conductors under tension and bending, Cigre Science Engineering 9 (2017) 5–7.
[43] F. Bussolati, M. Guiton, Y. Poirette, M. Martinez, P. Guidault, O. Allix, A new fully-detailled finite element model of spiral strand wire ropes for fatigue life estimate of a mooring line, International Conference on Ocean, Offshore and Arctic Engineering 38 (2019) 10.
[44] N. Buannic, P. Cartraud, G. L'Hostis, Homogénéisation de structures ou matériaux constitués de poutres, Colloque national en calcul des structures, Giens, France (1999).
[45] S. Sævik, H. Li, Shear Interaction and Transverse Buckling of Tensile Armours in Flexible Pipes, International Conference on Offshore Mechanics and Arctic Engineering Volume 4A: Pipeline and Riser Technology (2013).